05 Jul 2023

A Strong and Ductile Cobalt-Free Solid-Solution Fe30Ni30Mn30Cr10 Multi-Principal Element Alloy from Hot Rolling

Hans Pommerenke

Jiaqi Duan

Nathan Curtis

Victor DeLibera

et. al. For a complete list of authors, see https://scholarsmine.mst.edu/matsci_eng_facwork/2937

Recommended Citation

H. Pommerenke et al., "A Strong and Ductile Cobalt-Free Solid-Solution Fe30Ni30Mn30Cr10 Multi-Principal Element Alloy from Hot Rolling," *Journal of Alloys and Compounds*, vol. 948, article no. 169566, Elsevier, Jul 2023.
The definitive version is available at https://doi.org/10.1016/j.jallcom.2023.169566

Journal of Alloys and Compounds 948 (2023) 169566

Contents lists available at ScienceDirect

Journal of Alloys and Compounds

journal homepage: www.elsevier.com/locate/jalcom

A strong and ductile cobalt-free solid-solution $Fe_{30}Ni_{30}Mn_{30}Cr_{10}$ multi-principal element alloy from hot rolling

Hans Pommerenke [a], Jiaqi Duan [a,c], Nathan Curtis [a], Victor DeLibera [a], Adam Bratten [a], Andrew Hoffman [a,b], Mario Buchely [a], Ronald O'Malley [a], Haiming Wen [a,*]

[a] Department of Materials Science and Engineering, Missouri University of Science and Technology, Rolla, MO 65401, USA
[b] General Electric Global Research Center, Niskayuna, NY 12309, USA
[c] Warwick Manufacturing Group, University of Warwick, Coventry CV4 7AL, UK

ARTICLE INFO

Article history:
Received 9 December 2022
Received in revised form 18 February 2023
Accepted 6 March 2023
Available online 11 March 2023

Keywords:
High entropy alloy
Thermomechanical treatment
Inclusion analysis
Mechanical properties
Hot rolling
Multi-principal element alloy

ABSTRACT

Most of the face-centered cubic (FCC) multi-principal element alloys (MPEAs) developed thus far contain cobalt. For many applications, it is either required or beneficial to avoid cobalt, since cobalt has long-term activation issue (for nuclear applications), is expensive, and is considered a critical material. In addition, FCC structured solid-solution MPEAs tend to have relatively low strength. A FCC solid-solution $Fe_{30}Ni_{30}Mn_{30}Cr_{10}$ (at %) MPEA was fabricated via arc melting, followed by homogenization at 1100 °C for 12 h. The alloy was hot rolled at 1100 °C with a total reduction of up to 97 %. The microstructure was characterized and mechanical properties were investigated at various stages. Tensile testing showed that yield strength (YS) increased by 285–595 MPa and ultimate tensile strength (UTS) increased by 520–710 MPa. This increase in YS and UTS occurred with a total elongation (ductility) of 40 %. Meanwhile, hot rolling at high reductions led to evident decreases in size and area fraction of Mn-rich inclusions. Overall, after hot rolling, this FCC solid-solution MPEA is both strong and ductile.

1. Introduction

Though a relatively new field with most studies having been performed after 2005, MPEAs show a promise in a wide range of applications, owing to their high ductility, high strength, good corrosion resistance, and a strong resistance to radiation damage [1]. While MPEAs were originally designed and developed as single-phase equimolar alloys, many MPEAs reported more recently are non- equimolar. MPEAs have good properties due to a multitude of effects including the high-entropy effect, i.e., increased phase stability due to the high mixing entropy, which competes with the enthalpy of formation for secondary phases. Sluggish diffusion and lattice distortion also play a large role in stability of MPEAs. Sluggish diffusion is a result of the energy needed to break and form bonds as an atom diffuses throughout the matrix lattice with lattice distortion [2]. The possession of many attractive properties as mentioned earlier make investigation into different MPEAs lucrative as materials for applications in extreme environments such as nuclear reactors.

Nuclear reactors represent extremely harsh environments, owing to the presence of high temperature, high stress, intense irradiation, and corrosion by the coolant. Such environments pose enormous challenges to materials, which constitutes a materials science/engineering challenge. MPEAs have potential for improved performance and robustness in nuclear reactors, owing to improved stability and mechanical properties as well as enhanced resistance to irradiation [3] and corrosion [4]. For nuclear structural materials and fuel cladding, cobalt needs to be avoided, because of the creation of Co-60, which is very radioactive and has a long half-life. Most of the FCC structured MPEAs developed thus far contain Co, whereas only an extremely small number of FCC Co-free MPEAs have been reported [4–6]. A Co-free $Fe_{27}Ni_{28}Mn_{27}Cr_{18}$ MPEA (cold rolled) has been reported to possess an ultimate tensile strength (UTS) of ~630 MPa [5] with a total elongation (ductility) of ~37 % at room temperature; this alloy also exhibited good irradiation damage resistance [6]. Another Co-free $Fe_{40}Ni_{20}Mn_{20}Cr_{20}$ MPEA (cold rolled followed by annealing) exhibited an UTS of 1.34 GPa and total elongation of 23 % at cryogenic temperature of 77 K [7]; however, this MPEA had an UTS of ~1.00 GPa and total elongation of only ~7 % at room temperature.

While some HEAs possess both high strength and good ductility, many FCC structured MPEAs (especially solid-solution ones) suffer

* Corresponding author.
E-mail address: wenha@mst.edu (H. Wen).

https://doi.org/10.1016/j.jallcom.2023.169566
0925-8388/

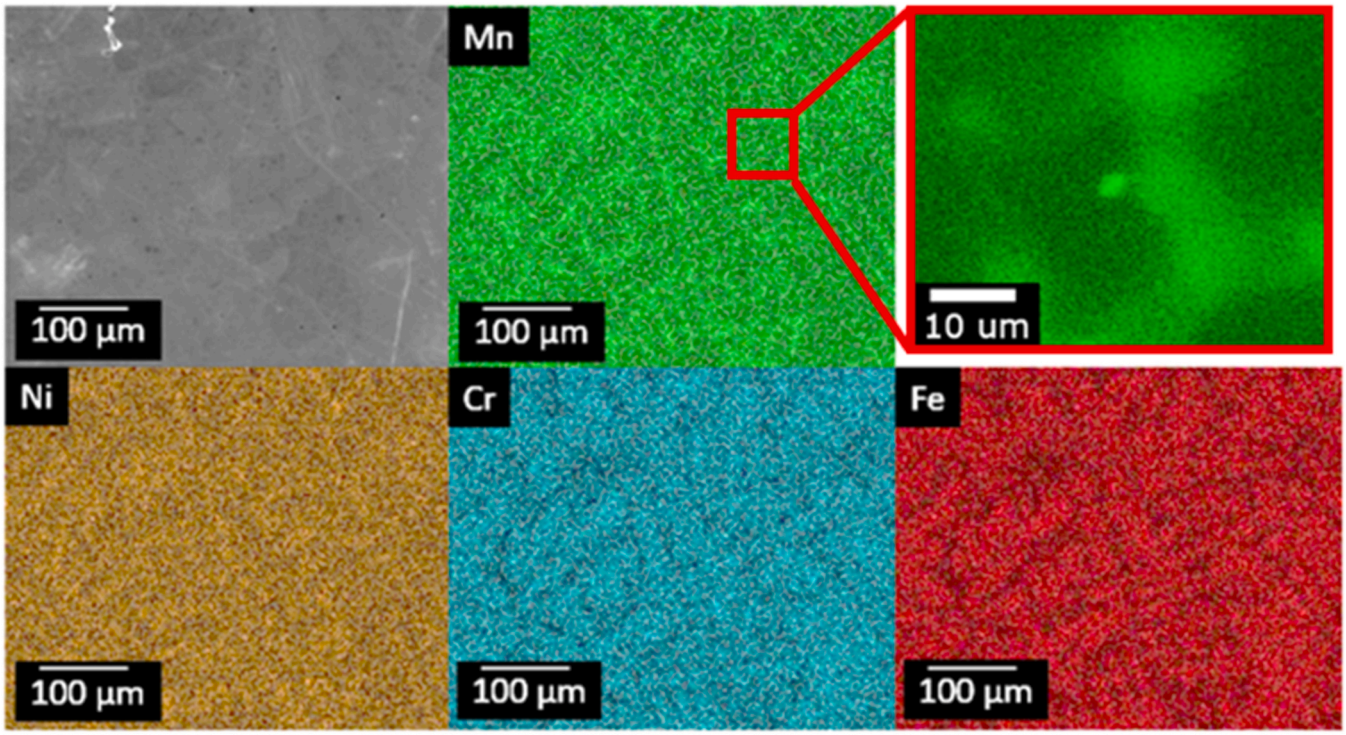

Fig. 1. SEM image and EDS elemental maps showing the as-cast microstructure: dendritic microstructure can be seen with Fe- and Cr-rich dendrites and Mn- and Ni-rich inter-dendritic areas. Mn-rich inclusion particles are small dark spots in the SEM image and can be seen as bright green points on the Mn map.

from poor strength [8]. One approach to enhancing the strength of these alloys is through grain refinement, which can be achieved using thermomechanical processing such as hot rolling. Many studies employ cold rolling as a step during processing of MPEAs, but little systematic work has been performed to study the microstructural and property evolution during hot rolling especially in ductile MPEAs. Mechanical rolling has been shown to refine the microstructure and increase strength [9,10]. The refined microstructures have also been linked to improved corrosion resistance [11].

In larger scale such as industrial manufacturing of alloys via melting and casting, inclusions are almost unavoidable. Laboratory production of alloys including MPEAs typically also results in inclusions in the alloys, although very few studies have addressed these inclusions or combated the formation or reduction of these inclusion particles. Inclusions have been observed in laboratory-produced Fe-Ni-Mn-Cr MPEAs [12]], although they were not specifically called out. Inclusions have been known to be the cause of failure in produced alloys. Thus, efforts are typically made to remove or reduce inclusions during industrial production of alloys. Rolling has been shown to change inclusion morphology and even allow the particle's elemental components to dissolve into the matrix [13].

The objectives of this study are to develop a strong and ductile FCC structured Co-free solid-solution MPEAs, as well as to provide insight into the effect of hot rolling on the microstructural evolution (including the grain structure evolution and the changes in inclusions) of a Co-free $Fe_{30}Ni_{30}Mn_{30}Cr_{10}$ MPEA. This particular MPEA was designed based on the Cantor alloy system with the removal of Co and the reduction of Cr content. The reduction of Cr content was motivated by two considerations: 1) to enhance the trend to form an FCC structure, which is beneficial to maintain an FCC matrix even after adding some precipitate-forming elements ($Fe_{30}Ni_{30}Mn_{30}Cr_{10}$ will be used as the matrix for precipitate-hardened MPEAs, which will be reported in separate publications); 2) to improve the corrosion resistance of the MPEA to molten salt, which will be reported in the future.

2. Experimental

The $Fe_{30}Ni_{30}Mn_{30}Cr_{10}$ studied was produced using pure metals (purity > 99.9 %) in a vacuum induction furnace, which was pumped down and backfilled with high purity argon three times to ensure a low oxygen content. The furnace was then held at a slightly positive pressure to ensure no air/oxygen could penetrate seals over the duration of the melting procedure. The melt procedure slowly ramped up the furnace to ensure no damage to coils and casting was carried out into a sand mold once all material was liquified. Homogenization was carried out on the cast for 12 hrs at 1100 °C in a muffle furnace. After the homogenization and subsequent cooling, the oxide layer on all sides were removed by machining.

The bulk homogenized sample was heated in a muffle furnace to 1100 °C. Hot rolling was then performed on the sample, with re-heating occurring after the sample temperature dropped below ~950 °C identified by the color of the hot metal. Reductions in thickness were made in 0.1 mm increments with three reductions per heating cycle. The sample was then transferred back to the furnace until it reached the temperature of 1100 °C again. Once the material had reached a desired thickness corresponding to a specific percent reduction, samples were cut off from the bulk material being rolled using an angle grinder while remaining within the temperature margin. Cut off sections were promptly quenched in water to room temperature while the bulk material was returned to the furnace for re-heating. After cut off, no further heat treatment was performed.

Tensile samples were cut using electrical discharge machining with a brass wire. Due to the limited sizes of sections of rolled material, mini-tensile sample dimensions were chosen with a gauge length of 3 mm and a gauge section of 1 × 1 mm. Tensile tests were performed using a setup optimized for mini-tensile samples and run with a strain gauge. Tensile samples from the 97 % rolling reduction were not able to be produced due to the samples curling up on themselves during cutting by EDM. Initial displacement rate was 0.005 mm/sec and after the strain gauge was removed increased to

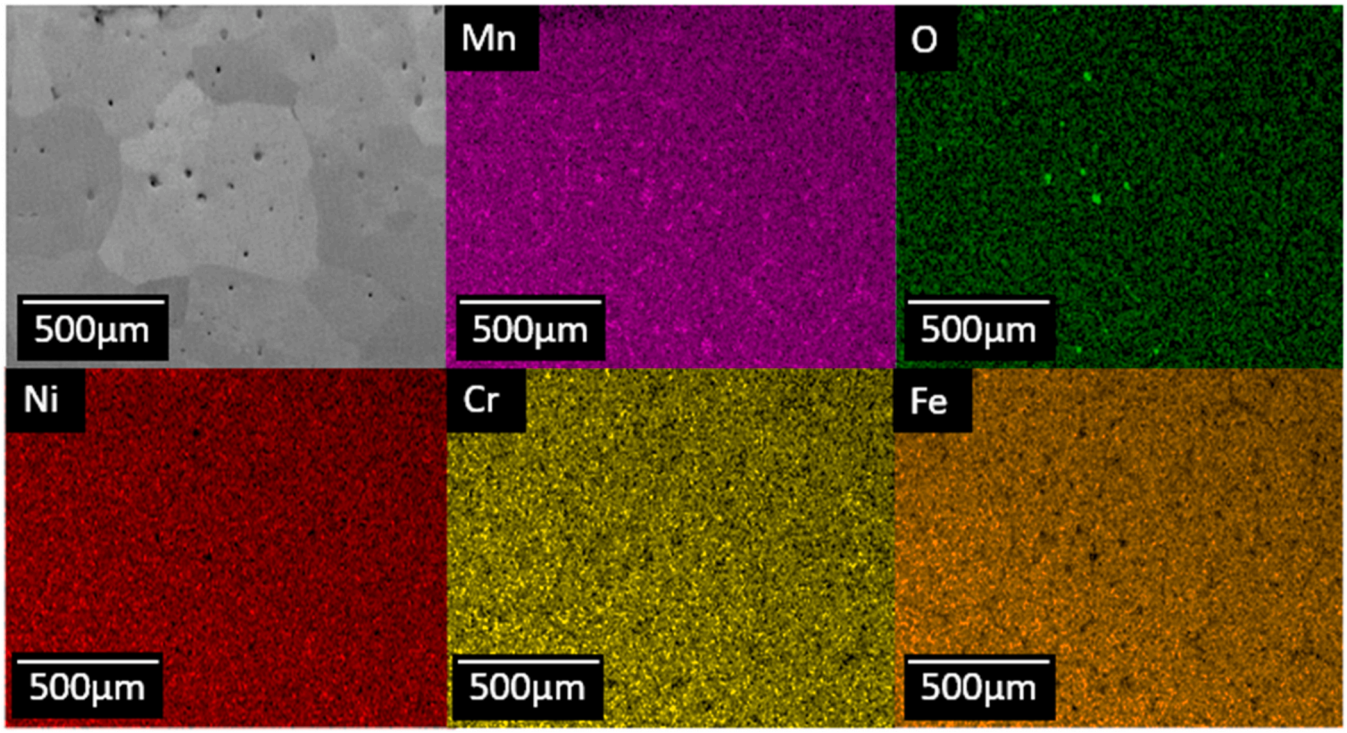

Fig. 2. SEM image and EDS elemental maps showing homogenized microstructure after 12 hr at 1100 °C: dendritic microstructure is removed; Some Mn-rich particles are visible in the Oxygen map due to Mn oxidizing after polishing.

0.02 mm/sec. The load frame used was an Instron 6800 tabletop load frame with a 5 kN loadcell attached to it. Hardness measurements on all samples was performed using a Struers Duramin 5 Vickers hardness tester. Electron backscatter diffraction (EBSD) was performed at 30 kV with a working distance of 5 mm for the objective lens and a working distance of 2.2 mm for the charge-coupled device camera. Electron dispersive spectroscopy (EDS) and focused ion beam (FIB) were also used. The controller software for EDS and EBSD was AZtecHKL from Oxford. For FIB, a gallium beam was used to cut into the high Mn particle. This sectioning was performed on a surface level particle of a fracture surface from the as-homogenized sample. All these techniques were performed using a Helios NanoLab 600 FIB scanning electron microscope (SEM).

A strengthening analysis was performed to determine the strengthening contributions from grain refinement as well as dislocation buildup. Grain size effect on strength (i.e., grain boundary strengthening) was analyzed using the Hall-Petch equation. X-ray diffraction (XRD) was carried out to estimate the dislocation density using peak broadening through the Williamson-Hall method. XRD was performed using a Philips MRD XRD ranging from 20 to 120° for 30 min.

3. Results

3.1. As-cast and homogenized microstructures

Fig. 1 shows the dendritic microstructure in the as-cast sample. Dendrites contain higher contents of Fe and Cr, and Mn and Ni segregation to the inter-dendritic regions can be observed. Dendrites are approximately 20–35 µm in width. In addition, Mn-rich particles are found in the as-cast sample. Work by Chen L. indicated that such particles were also present in powder metallurgy samples suggesting that they were not un-melted particles [14]. After homogenization, elements were homogeneously distributed, though some segregation to the grain boundaries can be observed in the Mn map, as revealed in Fig. 2. The oxygen map was added in this case to show the Mn particles that will be discussed later. These particles can also be observed in the BSE image in Fig. 2. The locations of the particles tend to appear as voids as the particles fall out of the matrix during sample preparation. This is most likely due to a significant mismatch of coefficient of thermal expansion between the particle and the matrix resulting in a loss of adhesion during sample cooling. Generally, these particles are in the range of 10–30 µm.

3.2. Microstructure evolution during hot rolling

The changes in microstructure due to hot rolling can be seen in Fig. 3. Fig. 3A–D display EBSD strain maps at 30 %, 60 %, 75 %, and 97 % reduction, respectively. Grain refinement is evident throughout the different rolling reductions. Greater reduction also results in internal strain inside grain interiors rather than just strain at the grain boundaries. The internal strain also can be linked to future new grain formation due to recrystallization during heating cycles. In Fig. 3a large unresolved/unindexed areas correspond to voids, which may be due to casting defects or owing to the falling of Mn particles during sample preparation. Due to the forging happening during hot rolling, casting defects between are closed and welded shut between Fig. 3a and 3b. At lower reductions, the recrystallization is already evident. At 60 % reduction, seen in Fig. 3b, the strain inside the grains is very low; at 75 % reduction, grain internal strain begins to build up. Grain refinement does not proceed homogenously. Instead, refinement occurs initially near prior grain boundaries, which exhibit a high degree of local deformation and accordingly a higher driving force for recrystallization. Even at 60 % reduction, although the grain refinement is more extensive, large grains still exist, with only small amounts of dislocations inside the grains. At 75 % reduction, the grain shape becomes much more equiaxed. At 97 % reduction in Fig. 3d a microstructure can be seen which has evident internal strain and no large grains can be observed.

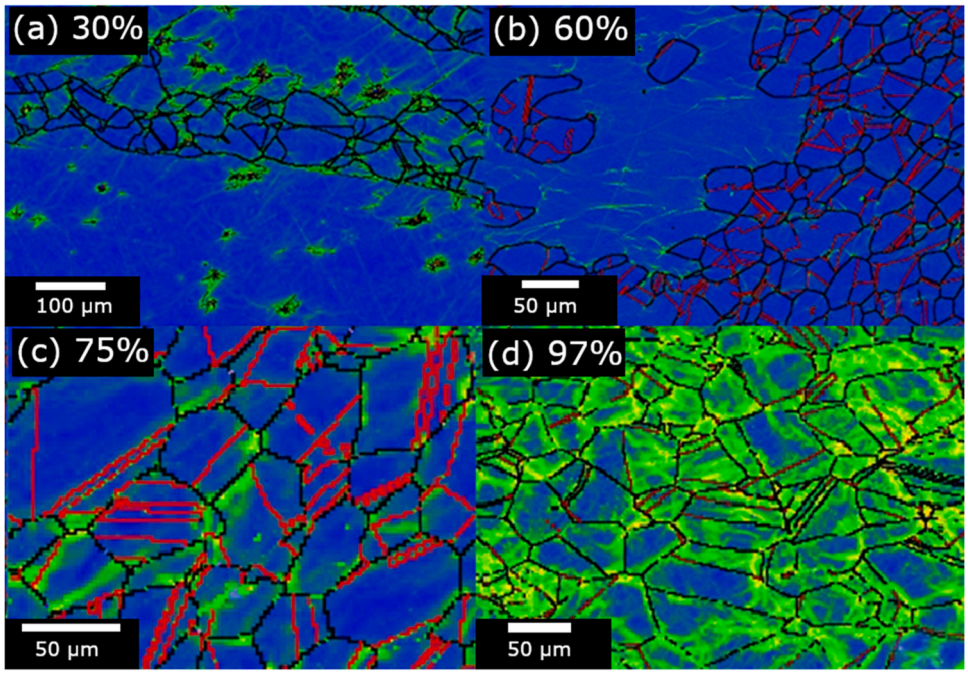

Fig. 3. EBSD strain map showing the microstructure evolution during rolling: (a) 30 % reduction, (b) 60 % reduction, and (c) 75% reduction. Grain sizes vary, with extremely large grains present at reductions of 30 % and 60 %. Noticeable internal strain buildup is only seen at high reduction percentages. A scale of Blue to yellow was used to show strain buildup though this strain is not absolute but relative to surrounding crystal missorienation. Red grain boundaries are twin boundaries with a range of 60 ± 3°. All other grain boundaries 15° + are shown in black. Low angle grain boundaries are not denoted in this figure.

3.3. Effects of rolling on mechanical properties

Tensile test results displayed in Fig. 4 show the effect of rolling on the tensile properties of the $Fe_{30}Ni_{30}Mn_{30}Cr_{10}$ MPEA. Strength increases of 60 MPa for YS and an increase in UTS of 62 MPa can be observed between the 30 % and 60 % hot rolled samples. Ductility increased in this time due to the reduction of casting porosity. The bimodal grain size distribution also allows the large grains to handle more deformation [15]. Typical Hall-Petch relation (effect of grain size on strength with smaller grain sizes resulting in higher strength) is observed with subsequent samples reducing in ductility but increasing strength. The only sample to break this trend is no reduction sample to 30 % reduction where casting defects have been closed. The 75 % reduction sample exhibits a yield strength of 595 MPa, a UTS of 710 MPa, a uniform elongation of 25 %, and an elongation-to-failure of 40 %. This sample is strong and ductile, for FCC structured solid-solution MPEAs.

3.4. Inclusion particle composition

The black spots in the SEM image in Fig. 2, as previously stated, correspond to voids left by particles that fell out during the polishing process. In Fig. 5a particle can be observed on a fracture surface from the homogenized sample. This particle was sectioned using a focused ion beam to determine the particle's internal chemistry without exposure to air. Table 1 shows the composition at different positions as measured by EDS. The results indicate that the particle is almost pure Mn. In addition, this particle has an attached tail

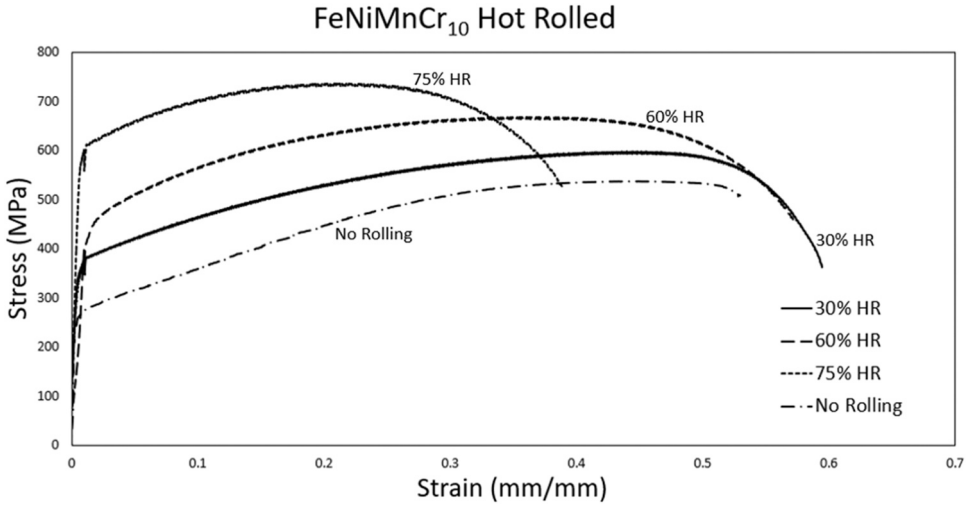

Fig. 4. Engineering stress-strain curves from tensile tests at different rolling reductions. Pre-rolling sample has a YS of 265 MPa and a UTS of 507 MPa at a ductility of 54 % while at 75 % reduction YS is 605 MPa and UTS is 710 MPa at 40 % ductility. While 97 % rolling reduction EBSD data are shown in Fig. 3, due to the small thickness (~1.2 mm) and internal strain in the sample, tensile samples were not able to be produced.

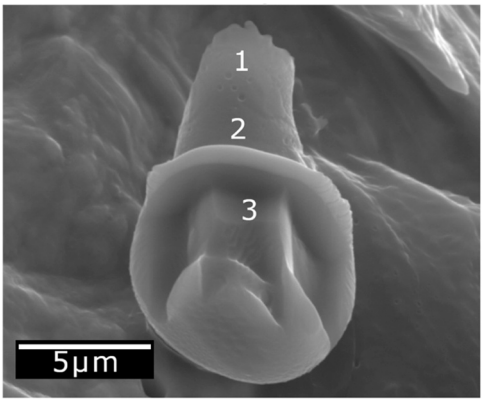

Fig. 5. SEM image of a Mn-rich particle on a fracture surface of the as homogenized tensile sample, which has been cut open using a focused ion beam to perform EDS to obtain the internal chemistry without any contamination by the outside atmosphere. The particle shown has the addition of a tail, but this is not common, and most particles are spherical without tails.

Table 1
Elemental composition of the Mn-rich particle at different locations of the particle (see Fig. 5), measured by EDS point scans. (*) Oxygen has been artificially added here to showcase that these particles are not MnO for positions 3 and the shell. These results indicate that the particle itself is effectively pure Mn. Shell is used for area 3 before the surface had been removed. Positions 1 and 2 are part of a Mn sulfide tail which while showcased in this figure is not common on most particles.

Position Elements	1 (wt %)	2 (wt %)	3 (wt %)	Shell (wt %)
O*	35.2	1.3		
Mn	29	55.9	97	95.11
S		39.1		
Fe	16.1	1.5		1.75
Ni	14.2	1.4	1.1	1.43
Cr	5.5	0.8	1.9	1.71

much like a MnS inclusion in steels, but this is an exception and almost all particles have only the round body without a tail. This particle was chosen to show that even particles with tails are effectively pure Mn.

3.5. Effect of hot rolling on Mn-rich particles

Rolling was also used as a technique for reducing both the size and volume/area fraction of the Mn-rich particles. Fig. 6 demonstrate changes to Mn-rich particles with increased hot rolling reduction. The particle morphology has also been changed to be slightly stretched in the direction of rolling. This phenomoenon of particle distortion only occurs at higher rolling percentages.

During rolling the Mn-rich particles were deformed and became elongated along the rolling direction. This phenomenon can be seen in Fig. 7. Fig. 7a and 7b shows a particle that has been deformed and elongated; the EDS map confirms that this is a Mn-rich particle. Another particle is displayed in Fig. 7c. The shape of the particle is from bottom left to top right, in line with the rolling direction. A majority of the particles have fallen out of the matrix during the polishing procedure, leaving an empty space on the surface. From the EDS maps, this particle seems to be almost pure Mn, and small parts of it remain attached to the matrix on the surface. It is likely that before polishing the particle had already been broken into pieces, and some pieces with weak bonding to the matrix easily fell off during polishing, whereas other pieces more strongly adhered to the matrix remained attached to the surface after polishing. It is surmised that these smaller particle parts may be re-dissolved into the matrix or may become too small to be detected by SEM.

Changes in particle diameter and area percentage can be seen in Fig. 8, which shows that both the area percentage and particle diameter are reduced at higher reductions of hot rolling. The changes in diameters though observable at lower reductions are not as evident and often are within error ranges of each other until higher percent reductions. After 75 % reduction, the average diameter was 3.0 µm, and it decreased to 2.2 µm as the reduction increased to 89 %; the value further decreased to 1.8 µm after a reduction of 97 %. Meanwhile, as rolling reduction increased, inclusion particle diameter distribution shifted to the left in Fig. 8, and area percentage of the particles decreased, indicating that hot rolling is effective in Mn-rich particle reduction.

3.6. Microstructural sources for strengthening

Sources for the strengthening in the hot rolled samples can be seen in Table 2. The average grain size initially decreases. Following work by Lehto. P, when calculating the average grain size, values from the 1st and 99th percentile were excluded, since those grains were either too small or too large, which may askew the average value significantly [16]. After initial grain size reduction (due to dynamic recrystallization), grain size reaches a minimum at 60 % reduction, and then starts to grow again (owing to grain growth at the rolling temperature). Dislocation density was determined using the Williamson Hall plot taken from XRD data of each rolling condition. The slope of each line is the microstrain, ε, and the y-intercept is equal to $K\lambda/D$, where K= 0.9 is a constant, λ = 0.15405 nm is the Cu Kα wavelength, and D is the crystallite size in nanometers. The

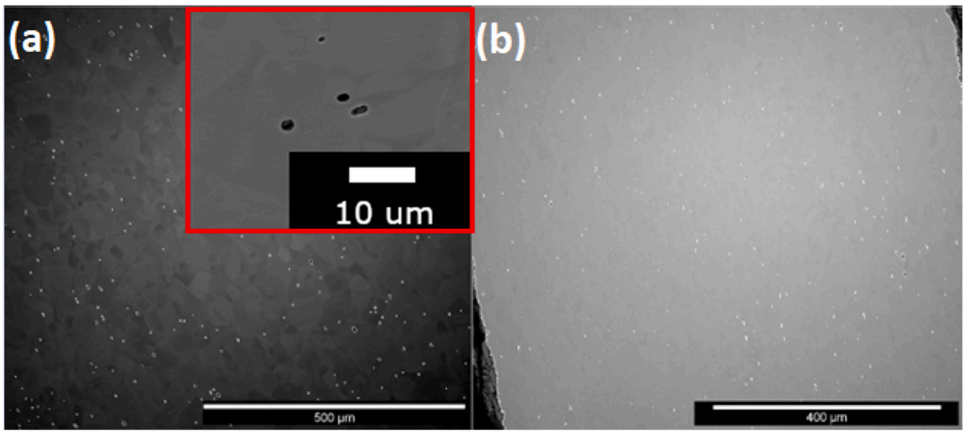

Fig. 6. SEM images showing distribution of Mn-rich particles in the hot rolled $Fe_{30}Ni_{30}Mn_{30}Cr_{10}$ MPEA: (a) 75 % rolling reduction the cutout in (a) shows the morphology of the particles; (b) 97 % rolling reduction. The particles exhibit white/bright borders. Qualitatively the number of particles is reduced with an increase in the rolling reduction.

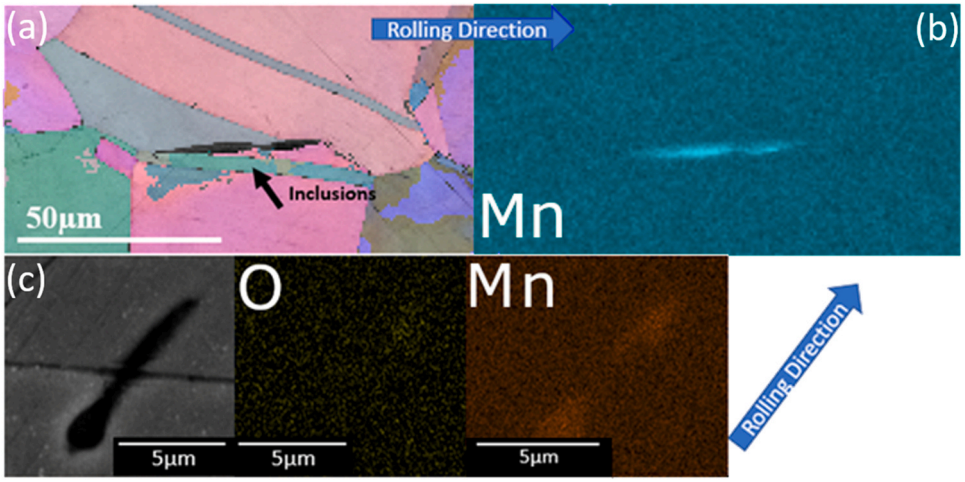

Fig. 7. SEM data showing Mn-rich inclusion particles in 99.5 % rolling reduction sample: (a) EBSD orientation map of an inclusion particle that has been deformed by rolling; (b). EDS map corresponding to (a) showing the Mn particle; (c) another particle deformed/elongated along the rolling direction, where the first sub-image is an SEM image, followed by O and Mn EDS maps.

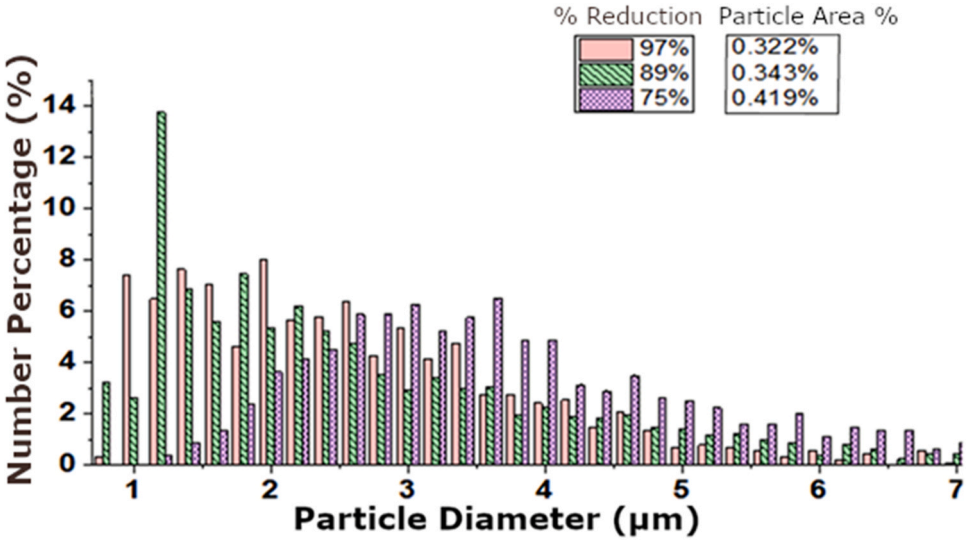

Fig. 8. Number percentage of particles with different diameters, after various hot rolling reduction.

dislocation density is then calculated using the equation $\rho = 2\sqrt{3} * \frac{\varepsilon}{Db}$, where ε is the microstrain, D is the crystallite size, and b is the Burger's vector, calculated as 0.256 nm. The dislocation density is too low for determination in 30 % and 60 %, resulting in non-real values, but the dislocation density clearly increases from 75 % to 97 % rolling reduction as can be seen in Table 2.

4. Discussion

4.1. Microstructural evolution due to hot rolling of $Fe_{30}Ni_{30}Mn_{30}Cr_{10}$ MPEA

Hot rolling was chosen as a grain refinement technique for this relatively ductile single-phase FCC solid-solution $Fe_{30}Ni_{30}Mn_{30}Cr_{10}$ MPEA. Initial grain refinement occurred along prior grain boundaries (Fig. 3a) where dislocations accumulated, resulting in recrystallization during deformation. The smaller grains that began to appear at higher rolling reductions in the hot rolled microstructure are much more equiaxed and little residual strain is left in the grain interior

Table 2
Shows the source of strengthening over different rolling reductions. Initial strengthening occurs due to grain size reduction. This changes after 75 % reduction as grain size grows slightly but dislocation buildup results in dislocation strengthening. Initial dislocation density numbers are incorrect due to the extremely low dislocation density leading to negative strain numbers in the Williamson-Hall plot.

Roll Reduction	30 %	60 %	75 %	97 %
Williamson-Hall Plot	y = −0.0012x + 0.0039	y = −0.0034x + 9E-05	y = 1.91E-04x + 4.40E-04	y = 1.97E-03x + 4.57E-03
Grain Size diameter (um)	2.34E + 01	1.76E + 01	3.26E + 01	3.20E + 01
Dislocation density (m^−2)	-4.57E + 14	-2.99E + 13	8.20E + 12	8.79E + 13

(Fig. 3b), suggesting that the grains experienced recrystallization [17]. The samples also underwent annealing due to being reheated to 1100 °C between rolling passes, and therefore static recrystallization was also possible. However, the increase in the strain inside the grains at high rolling reductions (evident in Fig. 3d) indicated that dynamic recrystallization was dominant since static recrystallization would result in reduced grain internal strain. The buildup of strain at higher reductions (≥ 75%)can be explained due to the reduced thermal mass of the sample resulting in faster cooling as well as a larger reduction in thickness causing more strain per pass.

4.2. Rolling effect on mechanical properties

In the present study, hot rolling has been shown to increase the strength of the $Fe_{30}Ni_{30}Mn_{30}Cr_{10}$ MPEA (Fig. 4). This strength enhancement is primarily due to the reduced grain size in the microstructure, which is known as the Hall-Petch relation [18]. Quantification of this relationship though is difficult as the bi-modal grain size distribution does not allow for a single grain size number to be used [19]. Rolling of very ductile materials such as aluminum shows similar behavior to that of $Fe_{30}Ni_{30}Mn_{30}Cr_{10}$ MPEA investigated in this study. Results from [20] showed small grains forming along the former grain boundaries as these are sites for dislocation accumulation and subsequent recrystallization static. In addition to grain refinement, the buildup of strain inside the grains (Fig. 3) at higher rolling reductions (≥ 75%)also improved the strength. However, this is considered a secondary contribution, since the hot rolling was performed at a high temperature of 1100 °C, and the accumulated dislocation density was anticipated to be low at such a high temperature.

4.3. Strengthening mechanisms

A strengthening analysis was performed to determine the strengthening mechanisms from hot rolling. Both the Hall-Petch relationship as well as dislocation strengthening were investigated to determine the main strengthening contributors. Grain size reduction plays a major role in the initial strength increases. The initial millimeter sized grains hamper efforts to determine grain size effect [16]. Excluding these large grains allows an average grain size to be determined reflective of the strength. Grain size reduction stops after 60 % rolling reduction due to the dynamic recrystallization occurring during hot rolling being balanced out by grain growth. Due to the increased pressure during higher rolling reduction and reduced time to reach rolling temperature again, dislocation buildup occurs at higher rolling reductions, making dislocation strengthening the main strengthening contributor.

4.4. Hot rolling effect on Mn-rich particles

Hot rolling was investigated as a process to reduce Mn-rich particles in the $Fe_{30}Ni_{30}Mn_{30}Cr_{10}$ MPEA. In steels, similar processes have shown promise in changing the morphology and count of MnS inclusions [21]. In steels, Mn-rich particles are often MnS or MnO. However, in this $Fe_{30}Ni_{30}Mn_{30}Cr_{10}$ MPEA, it is thought that these Mn-rich particles are pure Mn and they form during cooling – they precipitate out of a solid solution super saturated in Mn [22]. Such particles have also been observed in additively manufactured material as well, further supporting that these particles are precipitated out of a super saturated solution. Additionally, additively manufactured materials also show that these are not un-melted particles, rather they form during cooling after melting [14]. It is important to try to reduce such inclusion particles, as they have been shown to be the site for crack initiations and accordingly lead to failure in steel parts [23]. Similarly, it is beneficial to reduce inclusion particles in MPEAs, although such a topic has not really been studied previously. Results in Figs. 7 and 8 clearly indicated that the diameter and area percentage of Mn-rich particles in the $Fe_{30}Ni_{30}Mn_{30}Cr_{10}$ MPEA were reduced. The exact mechanisms for the reduction in particle diameter and area percentage are unknown, but it is conjectured that multiple factors play roles. Firstly, in order to accommodate the plastic deformation as a whole during hot rolling, strain accumulates near the particles, leading to large local strain. Secondly, the particles are fractured, especially at high strain (high rolling reductions), and thus reduced in size. Finally, locally the particles, especially the small parts, are slowly dissolved into the matrix due to the increased strain present in the matrix allowing for extended solubility or supersaturation of Mn in the matrix [24].

5. Summary and conclusions

A Co-free $Fe_{30}Ni_{30}Mn_{30}Cr_{10}$ MPEA, which is significant for applications requiring avoidance of Co, was developed, and fabricated via casting, homogenization, and hot rolling at 1100 °C. Tensile testing was performed on the alloy hot rolled to different reductions. Microstructure characterization was carried out, via SEM, EDS and EBSD. The main findings of this study are:

1. Hot rolling remarkably improved tensile properties of the alloy. The tensile strength increased with the increase of rolling reduction. When rolling reduction increased from 30 % to 60 %, yield strength increased from 390 to 450 MPa, and UTS increased from 590 to 650 MPa, while the ductility almost remained at ~60 %, which was owing to the bimodal grain size distribution in the hot rolled samples up to 60 % rolling reduction. At rolling reductions ≥ 75%, the grain structure became equiaxed, and the grain size distribution was much narrower. The sample with 75 % rolling reduction achieved a yield strength of 595 MPa, an UTS of 710 MPa, and a ductility of 40 %, representing a strong and ductile FCC structured solid-solution MPEA.
2. Hot rolling is an effective way to reduce the size and area fraction of Mn-rich particles, commonly seen in Mn-containing steels and MPEAs (even though largely neglected in previous studies on MPEAs). Mn-rich particles were deformed along the rolling direction, and fractured into smaller parts, which may be dissolved into the matrix at high rolling reductions.

CRediT authorship contribution statement

Hans Pommerenke: Conceptualization, Formal Analysis, Investigation, Data Curation Writing – Original Draft. **Jiaqi Duan:** Conceptualization, Methodology, Investigation, Data Curation, Writing – Review & Editing. **Nathan Curtis**: Investigation. **Victor DeLibera:** Investigation. **Adam Bratten:** Investigation. **Andrew Hoffman:** Methodology. **Mario Buckely:** Resources, Supervision. **Ronald O'Malley:** Resources. **Haiming Wen:** Conceptualization, Resources, Writing – Review & Editing, Supervision, Project Administration, Funding Acquisition.

Data availability

Data will be made available on request.

Declaration of Competing Interest

The authors declare that they have no known competing financial interests or personal relationships that could have appeared to influence the work reported in this paper.

Acknowledgements

This research was financially supported by the U.S. Nuclear Regulatory Commission Faculty Development Program (award number NRC 31310018M0044).

References

[1] D.B. Miracle, O.N. Senkov, A critical review of high entropy alloys and related concepts, Acta Mater. (2017), https://doi.org/10.1016/j.actamat.2016.08.081
[2] K.Y. Tsai, M.H. Tsai, J.W. Yeh, Sluggish diffusion in Co-Cr-Fe-Mn-Ni high-entropy alloys, Acta Mater. (2013), https://doi.org/10.1016/j.actamat.2013.04.058
[3] T. Shi, P.H. Lei, X. Yan, J. Li, Y. Di Zhou, Y.P. Wang, Z.X. Su, Y.K. Dou, X.F. He, D. Yun, W. Yang, C.Y. Lu, Current development of body-centered cubic high-entropy alloys for nuclear applications, Tungsten 3 (2021) 197–217, https://doi.org/10.1007/s42864-021-00086-6
[4] Y. Shi, B. Yang, P.K. Liaw, Corrosion-resistant high-entropy alloys: a review, Metals (Basel) 7 (2017) 1–18, https://doi.org/10.3390/met7020043
[5] Z. Wu, H. Bei, Microstructures and mechanical properties of compositionally complex Co-free FeNiMnCr18 FCC solid solution alloy, Mater. Sci. Eng. A 640 (2015) 217–224, https://doi.org/10.1016/j.msea.2015.05.097
[6] N.A.P.K. Kumar, C. Li, K.J. Leonard, H. Bei, S.J. Zinkle, Microstructural stability and mechanical behavior of FeNiMnCr high entropy alloy under ion irradiation, Acta Mater. 113 (2016) 230–244, https://doi.org/10.1016/j.actamat.2016.05.007
[7] B.B. Bian, N. Guo, H.J. Yang, R.P. Guo, L. Yang, Y.C. Wu, J.W. Qiao, A novel cobalt-free FeMnCrNi medium-entropy alloy with exceptional yield strength and ductility at cryogenic temperature, J. Alloy. Compd. 827 (2020) 1–7, https://doi.org/10.1016/j.jallcom.2020.153981
[8] Z. Li, S. Zhao, R.O. Ritchie, M.A. Meyers, Mechanical properties of high-entropy alloys with emphasis on face-centered cubic alloys, Prog. Mater. Sci. 102 (2019) 296–345, https://doi.org/10.1016/j.pmatsci.2018.12.003
[9] C.W. Tsai, Y.L. Chen, M.H. Tsai, J.W. Yeh, T.T. Shun, S.K. Chen, Deformation and annealing behaviors of high-entropy alloy Al0.5CoCrCuFeNi, J. Alloy. Compd. (2009), https://doi.org/10.1016/j.jallcom.2009.06.182
[10] B. Bay, N. Hansen, D. Kuhlmann-Wilsdorf, Microstructural evolution in rolled aluminium, Mater. Sci. Eng. A (1992), https://doi.org/10.1016/0921-5093(92)90002-I
[11] K.D. Ralston, D. Fabijanic, N. Birbilis, Effect of grain size on corrosion of high purity aluminium, Electrochim. Acta (2011), https://doi.org/10.1016/j.electacta.2010.09.023
[12] N.D. Stepanov, D.G. Shaysultanov, M.A. Tikhonovsky, G.A. Salishchev, Tensile properties of the Cr-Fe-Ni-Mn non-equiatomic multicomponent alloys with different Cr contents, Mater. Des. (2015), https://doi.org/10.1016/j.matdes.2015.08.007
[13] R. Li, M. Yao, W. Liu, X. He, Effects of cold rolling on precipitates in Inconel 718 alloy, J. Mater. Eng. Perform. 11 (2002) 504–508, https://doi.org/10.1361/105994902770343737
[14] L. Chen, Z. Li, P. Dai, P. Fu, J. Chen, Q. Tang, Effects of carbon addition on microstructure and mechanical properties of Fe50Mn30Co10Cr10high-entropy alloy prepared by powder metallurgy, J. Mater. Res. Technol. 20 (2022) 73–87, https://doi.org/10.1016/j.jmrt.2022.07.067
[15] M.J.N.V. Prasad, S. Suwas, A.H. Chokshi, Microstructural evolution and mechanical characteristics in nanocrystalline nickel with a bimodal grain-size distribution, Mater. Sci. Eng. A 503 (2009) 86–91, https://doi.org/10.1016/j.msea.2008.01.099
[16] P. Lehto, H. Remes, T. Saukkonen, H. Hänninen, J. Romanoff, Influence of grain size distribution on the Hall-Petch relationship of welded structural steel, Mater. Sci. Eng. A. 592 (2014) 28–39, https://doi.org/10.1016/j.msea.2013.10.094
[17] M.H. Alvi, S. Cheong, H. Weiland, A.D. Rollett, Recrystallization and texture development in hot rolled 1050 aluminum, Mater. Sci. Forum 467–470 (2004) 357–362, https://doi.org/10.4028/www.scientific.net/msf.467-470.357
[18] R.W. Armstrong, The influence of polycrystal grain size on several mechanical properties of materials, Metall. Mater. Trans. 1 (1970) 1169–1176, https://doi.org/10.1007/BF02900227
[19] N. Hansen, Hall-petch relation and boundary strengthening, Scr. Mater. 51 (2004) 801–806, https://doi.org/10.1016/j.scriptamat.2004.06.002
[20] J.J. Sidor, R.H. Petrov, L.A.I. Kestens, Microstructural and texture changes in severely deformed aluminum alloys, Mater. Charact. (2011), https://doi.org/10.1016/j.matchar.2010.12.004
[21] K.I. Yamamoto, H. Yamamura, Y. Suwa, Behavior of non-metallic inclusions in steel during hot deformation and the effects of deformed inclusions on local ductility, ISIJ Int 51 (2011) 1987–1994, https://doi.org/10.2355/isijinternational.51.1987
[22] Y. Tanaka, F. Pahlevani, S.C. Moon, R. Dippenaar, V. Sahajwalla, In situ characterisation of MnS precipitation in high carbon steel, Sci. Rep. 9 (2019) 1–12, https://doi.org/10.1038/s41598-019-46450-y
[23] G. Le Roy, J.D. Embury, G. Edwards, M.F. Ashby, A model of ductile fracture based on the nucleation and growth of voids, Acta Met. 29 (1981) 1509–1522, https://doi.org/10.1016/0001-6160(81)90185-1
[24] S. Sheibani, S. Heshmati-Manesh, A. Ataie, Structural investigation on nanocrystalline Cu-Cr supersaturated solid solution prepared by mechanical alloying, J. Alloy. Compd. 495 (2010) 59–62, https://doi.org/10.1016/j.jallcom.2010.02.034